



Pulsatile Flow Investigation in Development of Thoracic Aortic Aneurysm: An In-Vitro Validated Fluid Structure Interaction Analysis

C. W. Ong¹, F. Kabinejadian², F. Xiong¹, Y. R. Wong³, M. Toma⁴, Y. N. Nguyen¹, K. J. Chua⁵, F. S. Cui⁶, P. Ho⁷, H. Leo^{1†}

¹ Department of Biomedical Engineering, National University of Singapore, Singapore

² Department of Biomedical Engineering, Tulane University, New Orleans, LA, USA

³ Biomechanics Laboratory, Singapore General Hospital, Singapore

⁴ Department of Mechanical Engineering, School of Engineering & Computing Sciences, New York Institute of Technology, New York, USA

⁵ Department of Mechanical Engineering, National University of Singapore, Singapore

⁶ Institute of High Performance Computing, A*STAR, Singapore 138632, Singapore

⁷ Department of Cardiac, Thoracic & Vascular Surgery, National University Health System, Singapore

†Corresponding Author Email: bielhl@nus.edu.sg

(Received October 20, 2018; accepted January 26, 2019)

ABSTRACT

Thoracic aortic aneurysm (TAA) is a severe cardiovascular disease with a high mortality rate, if left untreated. Clinical observations show that aneurysm growth can be linked to undesirable hemodynamic conditions of the aortic aneurysm. In order to gain more insight on TAA formation, we developed a computational framework in vitro to investigate and compare the flow patterns between pre-aneurysmal and post-aneurysmal aorta using a deformable wall model. This numerical framework was validated by an in vitro experiment accounting for the patient-specific geometrical features and the physiological conditions. The complex flow behaviors in the pre-aneurysmal and post-aneurysmal aorta were evaluated experimentally by particle image velocimetry (PIV). Our experimental results demonstrated flow behaviors similar to those observed in the fluid-structure interaction (FSI) numerical study. We observed a small vortex induced by the non-planarity of pre-aneurysmal aorta near the aortic arch in pre-aneurysmal aorta may explain the aneurysm formation at the aortic arch. We found that high endothelial cell action potential (ECAP) correlates with the recirculation regions, which might indicate possible thrombus development. The promising image-based fluid-structure interaction model, accompanied with an in vitro experimental study, has the potential to be used for performing virtual implantation of newly developed stent graft for treatment of TAA.

Keywords: Thoracic aortic aneurysm; Particle image velocimetry; Thrombus; Fluid structure interaction (FSI); Hemodynamics.

NOMENCLATURE

D_{ijkl}	Lagrangian elasticity tensor	w	velocity components in z direction
k	constant of proportionality	α	Womersley Number
\mathbf{n}	normal vector	${}^F\Omega(t)$	moving spatial domain in which the fluid is defined
p	pressure	${}^S\Omega(t)$	structural domain at time t
Re_c	Critical Reynold number	ε_{kl}	structural strain tensor
T	time period of the flow cycle	ρ	density
u	velocity components in x direction	μ	viscosity
\mathbf{u}	velocity vector of the fluid-structure interface	$\boldsymbol{\sigma}$	stress tensor
v	velocity components in y direction	σ_{ij}	structural stress tensor
\vec{V}	fluid velocity vector	τ_w	WSS vector

1. INTRODUCTION

Thoracic aortic aneurysm (TAA) is the result of dilatation of aortic wall. Excessive dilatation can cause potentially fatal rupture of aneurysm, if left untreated (Sekhar and Heros, 1981). Aneurysm rupture could be (or has traditionally been) predicted based solely on its diameter (e.g., >5.5 cm); however, this method could be inaccurate (Elefteriades and Farkas, 2010). The pathogenesis of TAA formation and rupture is not yet fully understood, but it is widely accepted that hemodynamic changes play an important role in determining the disease progression (Biasetti *et al.*, 2011; Finol and Amon, 2001).

Hemodynamic changes have been correlated with thrombus formation. The changes of flow pattern change the wall shear stress (WSS) which is accepted to activate the platelets, ultimately leading to thrombus formation. Different hemodynamic metrics have been proposed to evaluate the WSS threshold for the risk of thrombosis, such as oscillatory shear index (OSI) and time-averaged wall shear stress (TAWSS). Arzani *et al.* showed that low OSI (<0.1) correlates well with risk of thrombus formation (Arzani *et al.*, 2014), while other research showed that low TAWSS can be linked to aneurysm expansion and thrombosis in the abdominal aortic aneurysm (AAA) (Doyle *et al.*, 2014; Zambrano *et al.*, 2016). Recently, endothelial cell action potential (ECAP) has been used to evaluate the thrombotic susceptibility in the aortic aneurysm (Di Achille *et al.*, 2014; Drewe *et al.*, 2017). Kelsey *et al.* showed, by a computational fluid dynamics (CFD) study, that high ECAP can promote thrombosis in the AAA (Kelsey *et al.*, 2017).

Image-based CFD is an attractive option that could provide hemodynamic information based on the patient's anatomy which can be otherwise difficult to assess *in vivo* (Kabinejadian *et al.*, 2015; Kabinejadian *et al.*, 2016; Steinman, 2002). Majority of CFD studies either used idealized geometry (Shahcheraghi *et al.*, 2002; Soudah *et al.*, 2012) or patient's geometry with a rigid wall (Tan *et al.*, 2009b; Tse *et al.*, 2011; Wen *et al.*, 2010) to investigate the flow field in aortic aneurysm. Although there are only a few fluid structure interaction (FSI) studies focused on aortic aneurysm (Borghetti *et al.*, 2008; Chandra *et al.*, 2013; Rissland *et al.*, 2008; Scotti *et al.*, 2008; Xenos *et al.*, 2015), the AAA geometries used in these studies are different from that of thoracic aortic aneurysm (TAA), which renders them incomprehensive for understanding the complex flow patterns in thoracic aortic aneurysm. To the best of our knowledge, only in Tan *et al.*'s study (Tan *et al.*, 2009b) the thoracic aortic aneurysm model included a coarctation (a narrow region before the aneurysm); this is while the flow field is influenced by the location of coarctation rather than only the aortic aneurysm.

In this paper, we present the results from two

compliant phantoms under pulsatile flow conditions for the comparison of flow field under fully coupled two-way FSI scheme. The 3D aneurysm model was constructed from the computed tomography (CT) images to preserve the patient-specific geometrical features. The validation was done by comparing the computed velocity fields with particle image velocimetry (PIV) measurements from an *in vitro* flow loop setup with equivalent flow and pressure waveforms applied as boundary conditions in the CFD simulations.

2. MATERIALS AND METHODS

2.1 Patient-Specific Model Construction

Two phantom models were constructed for the FSI simulation and *in vitro* experiment. The post-aneurysmal model (Fig. 1a) was reconstructed from a TAA patient's CT scan, using Mimics (Materialise, Leuven, Belgium). This model included the TAA and three superior arterial branches, namely, the brachiocephalic artery (BRA), the left common carotid artery (LCA), and the left subclavian artery (LSA). The diameter of the aneurysm sac was measured as 37.35 mm from the CT image. A pre-aneurysmal model was generated from the post-aneurysmal model by removing the enlarged portion of the TAA. A wall geometry with 2 mm thickness was generated by removing the inner lumen. Subsequently, both the wall and lumen geometries were imported into ANSYS Workbench (ANSYS, Inc., Canonsburg, PA, USA) for the FSI study.

The geometric dimensions of aorta are listed in Table 1.

Table 1 DIMENSIONS of the inlet and outlets

Location	Radius (mm)
Aortic inlet	17.662
Descending aorta outlet	14.352
BRA	6.211
LCA	4.177
LSA	3.493

2.2 Numerical Setup

ANSYS Workbench was utilized to facilitate the FSI simulation involving FLUENT and Transient Mechanical. Mesh sensitivity test was performed to confirm that the results were independent of further mesh refinements with less than 2% deviation of velocity among different mesh sizes, which was deemed acceptable (Menichini *et al.*, 2018).

The governing equations used in this coupling scheme (Wang and Li, 2011) are listed as Eqs. (1)-(6).

Flow continuity equation

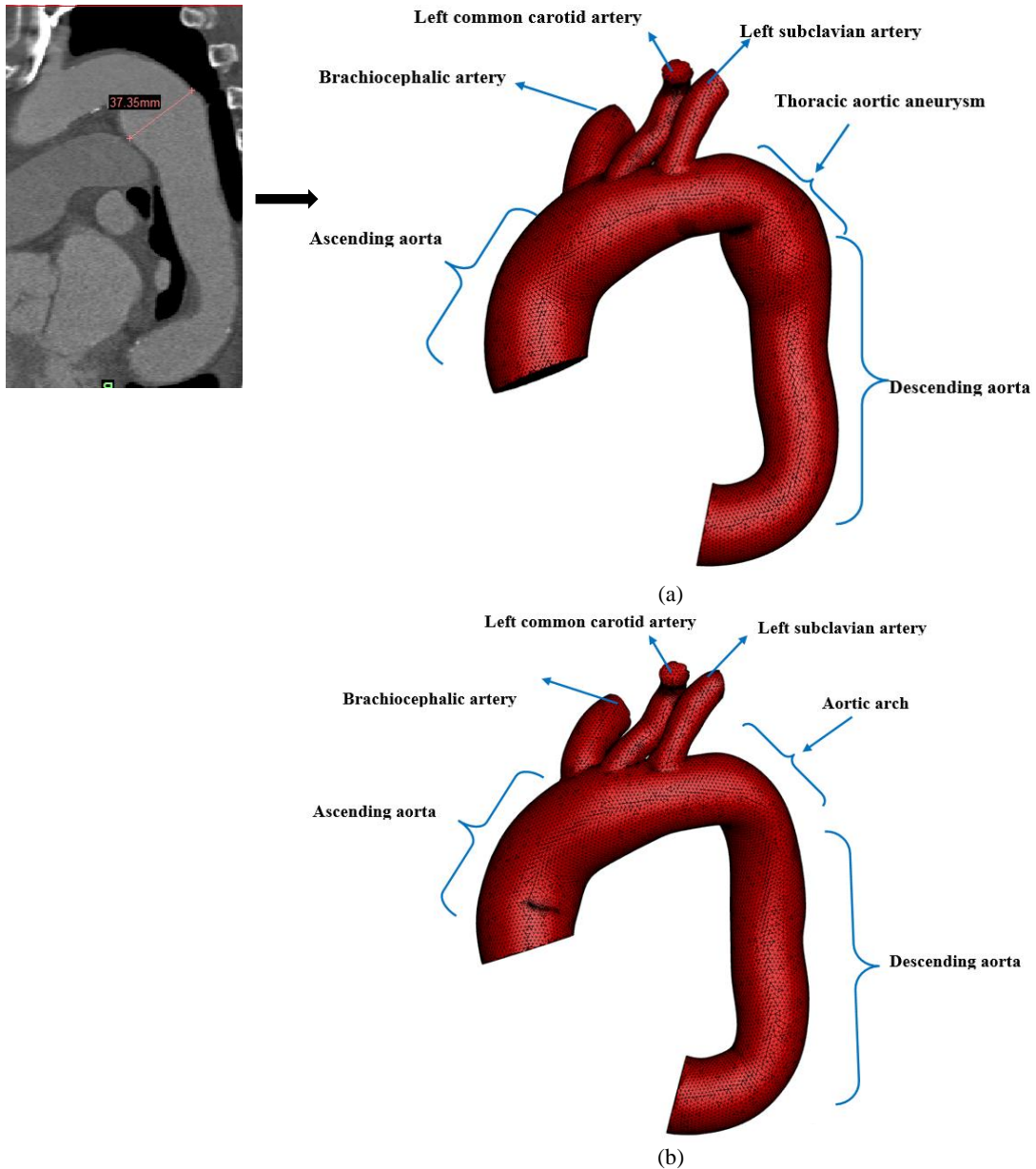


Fig. 1. Reconstruction of the 3D model from CT images (a) post-aneurismal aorta (b) pre-aneurismal aorta.

$$\nabla \cdot \vec{V} = 0 \quad (1)$$

Flow momentum equation

$$\frac{\partial}{\partial t}(\rho \vec{V}) + \rho(\vec{V} \cdot \nabla)\vec{V} = -\nabla p + \rho \vec{g} + \mu \nabla^2 \vec{V} \quad (2)$$

in $^F\Omega(t)$

where \vec{V} is the fluid velocity vector described by the velocity components u, v, w in x, y and z directions while $p, \rho,$ and μ represent, respectively, the pressure, density, and viscosity of the fluid. $^F\Omega(t)$ represents the moving spatial domain in which the fluid is define Structural momentum equation

$$\frac{\partial \sigma_{ij}}{\partial x_i} + f_i = \rho_p \frac{\partial u_i}{\partial t} \quad \text{in } ^S\Omega(t) \quad (3)$$

Structural constitutive equation

$$\sigma_{ij} = D_{ijkl} \varepsilon_{kl} \quad \text{in } ^S\Omega(t) \quad (4)$$

where $^S\Omega(t)$ is the structural domain at time $t,$ σ_{ij} is the structural stress tensor, D_{ijkl} is the Lagrangian elasticity tensor, and ε_{kl} is the structural strain tensor.

Coupling boundary conditions mandate equal velocity and pressure for both domains at the fluid-structure interface:

$$\mathbf{u}_f = \mathbf{u}_s \quad (5)$$

$$\boldsymbol{\sigma}_f \cdot \mathbf{n}_f = \boldsymbol{\sigma}_s \cdot \mathbf{n}_s \quad (6)$$

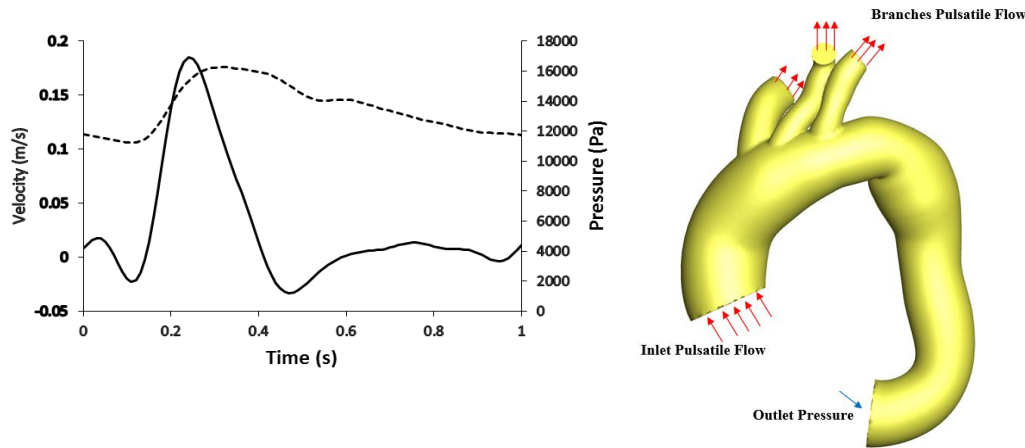


Fig. 2. Time-dependent inlet velocity (solid line) and pressure waveforms (dashed line) adopted from (Olufsen *et al.*, 2000; Tse *et al.*, 2011).

where σ , \mathbf{n} and \mathbf{u} are the stress tensor, normal vector, and velocity vector of the FSI interface, respectively.

2.3 Boundary Conditions

A time-dependent flow profile was prescribed at the ascending aorta inlet while the descending aorta outlet was formulated with pressure waveform through user-defined function in ANSYS FLUENT as shown in Fig. 2. These waveforms, adopted from Olufsen *et al.*'s (Olufsen *et al.*, 2000; Tse *et al.*, 2011) work, have been tested in various experimental studies (Fung, 2013; Pedley, 2003) and frequently used in simulating blood flow behaviors in both diseased and healthy models in various studies (Drewe *et al.*, 2017; Li and Kleinstreuer, 2006; Li and Kleinstreuer, 2007; Mesri *et al.*, 2017; Tse *et al.*, 2011; Wolters *et al.*, 2010). The outlets of superior branches were formulated with velocity profiles, measured from the experimental setup, ranging from 4%-6% of the total flow volume, subjected to their radius (Table 1). For the solid domain, all the inlet and outlets were fixed in all degrees of freedom. Both models were assumed to initially be in a zero stress state. A fixed time-step of 0.02 s was used in this study. Ten cycles, each lasting 1 second, were conducted, and only the results obtained in the final cycle were used for analysis. The convergence criteria were set to 10^{-5} for both continuity and velocity residuals (Zhang *et al.*, 2015).

Maximum Reynolds number for pre-aneurysmal aorta was 1800 and for post-aneurysmal aorta was 2801, calculated based on the cross-sectional average velocity (V_{ave}) at a section with the largest hydraulic diameter at the peak systole. A critical Reynolds number has been proposed in the literature (Morris *et al.*, 2005) in the form of $Re_c = ka$ to assess different flow conditions, with k being the constant of proportionality, ranging from 250 to 1000, and a the Womersley number. The Womersley number for pre-aneurysmal aorta was 9 and for post-aneurysmal aorta was 11, calculated based on the angular frequency, maximum hydraulic diameter, and kinematic viscosity. In our models, Re_c ranged from

2250 to 11000. Since the maximum Reynolds number in these models were lower than the maximum value of critical Reynolds number, the flow in our models for pre-aneurysmal aorta and post-aneurysmal aorta was formulated as laminar flow.

2.4 Material Properties

The blood density was set to 1050 kg/m³ with the dynamic viscosity set to 0.0035 Pa·s (Zhang *et al.*, 2014). The aortic wall was formulated as nearly incompressible, using linear elastic material with isotropic Young's Modulus as suggested in published literature (Gao *et al.*, 2006; Lantz *et al.*, 2011). The density of aortic wall was set to 1080 kg/m³ while the Poisson's ratio was set to 0.499 consistent with the literature (Lantz *et al.*, 2011; Wolters *et al.*, 2005). The wall stiffness is always subjected to specific parameters and a universal value does not exist (Lantz *et al.*, 2011). Here in this paper, the development of aortic aneurysm was investigated in-vitro. Phantom models of aorta were fabricated using silicone with Young's modulus of 2MPa, which is close to that of aorta.

2.5 Quantities of Interest

Endothelial action cell potential (ECAP) was chosen to quantify the artery wall's degree of thrombotic susceptibility (Kelsey *et al.*, 2017). That is a ratio of oscillatory shear index (OSI) and time-averaged wall shear stress (TAWSS). The expressions for TAWSS, OSI, and ECAP are given by Eqs. (7)-(9).

$$TAWSS = \frac{1}{T} \int_0^T |\bar{\tau}_w| dt \quad (7)$$

$$OSI = \frac{1}{2} \left(1 - \frac{\left| \int_0^T \bar{\tau}_w dt \right|}{\int_0^T |\bar{\tau}_w| dt} \right) \quad (8)$$

$$ECAP = \frac{OSI}{TAWSS} \quad (9)$$

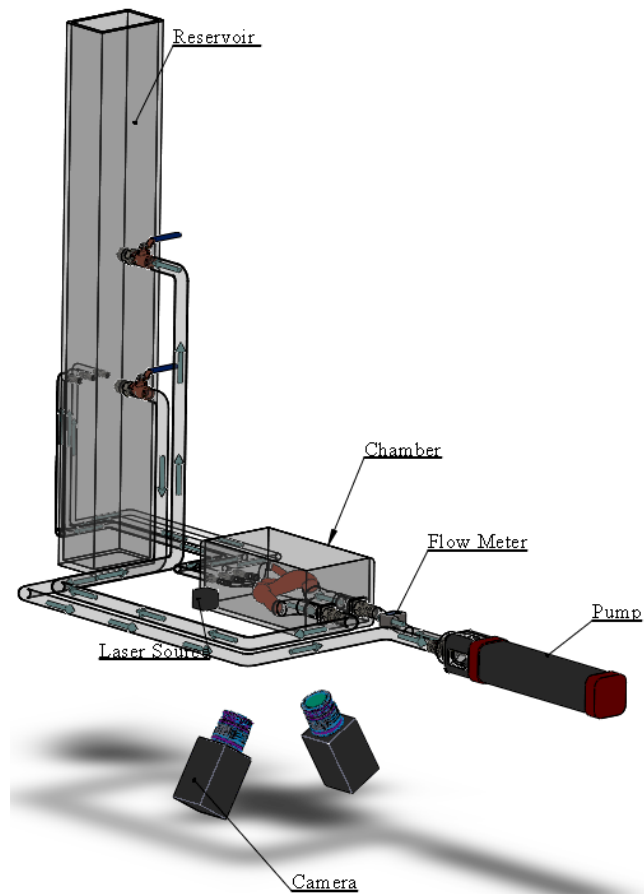


Fig. 3. Schematic of the flow loop with 3D PIV.

where τ_w is the WSS vector, and T is the time period of the flow cycle.

2.6 Experimental Setup

2.6.1 Compliant Phantom Model

The geometry of the phantom used in this study was first printed out by a 3D printer (Objet Connex 260, Stratasys, Edina, MN, USA) using acrylonitrile butadiene styrene (ABS) material. PDMS material (Sylgard 184, Dow Corning, Barry, UK) was then used to construct a mold from the 3D model. The mold was then filled with melted Isomalt to form a cast. After the Isomalt was hardened, the cast was taken out from the PDMS mold and coated with VTV750 silicone rubber. In order to generate a uniform thickness for the compliant phantom, the coating process on the Isomalt cast was performed while it was rotating continuously at 127 rpm using a direct current (DC) motor. After the silicone rubber was cured overnight, the Isomalt cast was dissolved in de-ionized water, obtaining the compliant patient-specific phantom model. The pre-aneurysmal aorta phantom model was made using the same procedure.

Prior to the *in vitro* study, we carried out uniaxial testing to obtain the Young's modulus of the VTV750 silicone rubber to be used in the simulation. Following the method proposed by Corbett *et al.* (Corbett *et al.*, 2010), ten Type 2 dumb-bell samples with 2mm wall thickness were made of VTV750

silicone rubber and tested on an Instron testing machine with a 1kN load cell in accordance with BS ISO 37. Precondition loading was also performed by deforming the gauge length by 40% ten times before conducting an actual test. This procedure was applied to preserve the stress-strain response of the material.

2.6.2 Flow loop Setup

Schematic of the flow loop setup with the phantom model is shown in Fig. 3. The pulsatile flow was created using a piston pump (SuperPump AR series, ViVitro Labs Inc., Victoria, BC, Canada) generating the inlet velocity profile with the flow rate of 4 L/min at the frequency of 1Hz, extracted from the literature. The connections between the rigid inlet and outlet sections of the acrylic chamber were fixed with hose clips that mimicked the set constraints applied in the FSI model. Both compliant phantoms were connected to two fluid reservoirs through valves of different sizes that created resistance. The elevation of the working fluid in the reservoir was adjusted in order to mimic human aortic pressure. An ultrasonic flow meter (ME16PXL, Transonic Systems Inc., Ithaca, NY, USA) was used to measure the flow rate at the ascending aortic inlet to ensure it matched the inlet condition in the numerical model. The flow rate in the superior branches was measured by another ultrasonic flow meter (ME10PXN). A pressure catheter was used (Mikro-Tip SPR-340S, Millar

Instruments Inc., Houston, TX, USA) to measure the pressure at the descending aortic outlet so that it matches the pressure outlet condition in the numerical model. A solution mixture of 40% glycerin and 60% water by volume with a density of 1050 kg/m³ and dynamic viscosity of 3.5 mPa·s at 23°C was made and verified using a Cannon-Fenske Routine viscometer to ensure the blood viscosity value was consistent with that used in the numerical model.

2.6.3 Particle Image Velocimetry (PIV)

A PIV system setup is built on three main components; an illumination source, an image acquisition system, and tracer particles. A 15-Hz Q-switched, pulsed Nd:YAG laser (NANO S35, Litron Lasers, Rugby, UK) with a wavelength of 532 nm at energy of 30 mJ was used as a light source to produce a 1mm-thick light sheet to illuminate the flow field in the chamber and the phantom model. Two charge-coupled device (CCD) cameras (Imager pro X, LaVision, Goettingen, Germany) with a spatial resolution of 1600×1200 pixel² were used to record images at a maximum rate of 12 Hz. The CCD cameras were fixed with a Scheimpflug mount (Model 1108196, LaVision, Germany) to ensure that they were focused at the area of interest. Cross-correlation algorithm (Davis, Version 8.3, LaVision, Germany) with iterative window sizing scheme was utilized to derive the displacement velocity vectors, starting with interrogation area of 128×128 pixels² to final interrogation window of 64×64 pixels², overlapped by 50%. A pulse separation optimizer was used to adjust the separation time at each phase of the cardiac cycle, ranging from 300 μs to 1000 μs during the systolic and diastolic phases to capture the flow pattern accurately. 150 measurements were taken at each time-point to obtain statistical convergence for a stable velocity vector.

3. RESULTS

3.1 Comparison of flow and Pressure Waveforms at Inlet and Multiple Outlets

Fig. 4. compares the simulated and measured flow and pressure waveforms at different locations in the two phantom models. The shapes and magnitudes of the simulated and measured waveform matched well throughout the cardiac cycle. The mean difference between the simulated and measured flow rates is 0.1 cm³/s, which is 1% of the mean flow rate (10 cm³/s). The mean difference between the simulated and measured pressure is 2.5 mmHg, which is 2.5% of the mean pressure (100 mmHg).

3.2 Comparison of flow Patterns Between the FSI and PIV Results in the Aneurysm

To better distinguish the flow patterns between the pre-aneurismal and post-aneurismal aorta, we focus our observation on four time-points over the entire cycle. These four different stages are most interesting to observe as regards to the complex flow behavior in the aorta. Measurements were taken at parallel planes, as indicated in Fig. 5. Six cross-sectional planes over the pre-aneurismal and eight

cross-sectional planes in the post-aneurismal aorta were selected for hemodynamic interrogation. Different number of measurement planes in the two models is due to the size of aneurysm being larger than normal aortic arch. The analysis of the results from the two models in the selected plane as shown in Fig. 5 is presented in this paper.

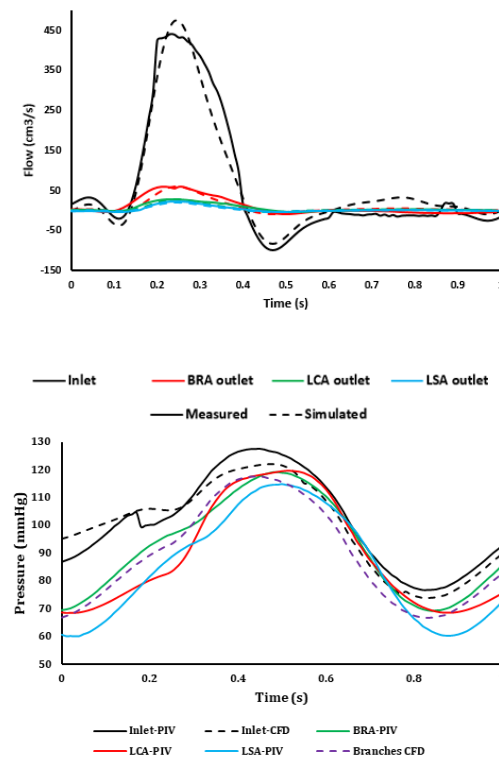


Fig. 4. Measured (continuous) versus simulated (dashed line) flow and pressure at various locations in the phantom models.

The flow velocity fields in the pre-aneurismal aorta model obtained by numerical and experimental methods are presented in Fig. 6. During the early systole (Fig. 6a), a significant forward flow was observed from the ascending aorta into the aortic arch. A high-velocity region at the inferior of the aortic arch was found where no flow separation was detected. A similar flow phenomenon was found at the mid-systole (Fig. 6b) with a good matching between the PIV and numerical results. In the late systole (Fig. 6c), a small vortex was detected near the inferior wall of the aortic arch, due to the interaction of forward and reversed flows from the descending aorta in both models. In the early diastole (Fig. 6d), the small vortex remained near the inferior wall of the aortic arch with a lower velocity profile.

Fig. 7(a)-(d) compares the experimental and simulated velocity distributions along X and Y directions at the cross-sectional plane Z=0.009 m for the aortic arch in the pre-aneurismal model. The velocity comparisons at the peak systole and early diastole reveal negligible discrepancies between the experimental and computational results. The CFD calculated velocities showed an average deviation of

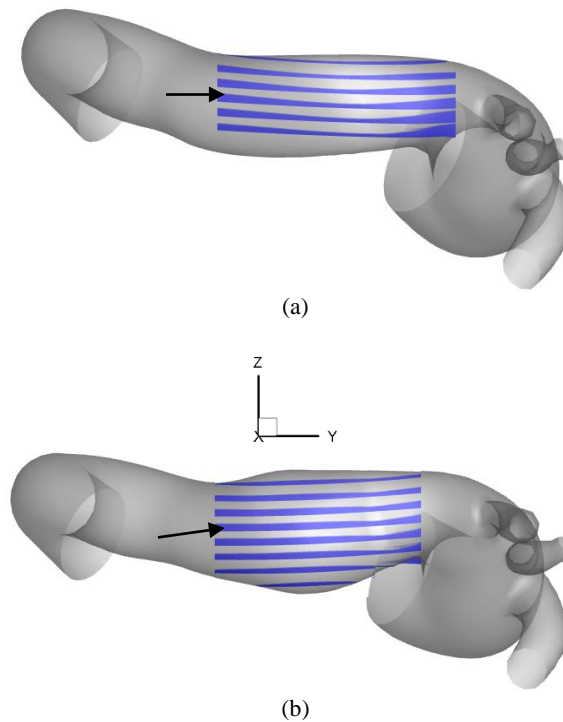


Fig. 5. Overview of the planar cross sectional planes used for the comparison between the CFD and PIV velocity quantifications. The plane pointed by the arrow is the selected plane for presentation. There is 3mm distance between adjacent planes. (a) pre-aneurismal aorta (b) post-aneurismal aorta.

5%-14% from the experimentally measured velocities during the peak systole while there is an average deviation of 15%-20% between CFD simulated velocities and PIV experimental measurements during early diastole.

The flow behavior in the post-aneurismal aorta was more complex than that in the pre-aneurismal aorta, as described in Fig. 8. The enlarged portion of the aorta (i.e., the aneurysm) disrupted the fast forward flow which was observed in the pre-aneurismal aorta. During the early systole (Fig. 8a), a high-velocity profile was found closer to the inner wall of curvature. However, this high velocity stream, present in the inner wall of curvature, disappeared in the aneurysmal sac which can be associated to the Bernoulli principle, whereby for irrotational flow, the velocity magnitude is inversely proportional to the radius of curvature of the streamline (Tan *et al.*, 2009a; Wood, 1999). A similar flow pattern was present at the mid-systole (Fig. 8b), but with the extension of high velocity streamline, since the stronger accelerating flow enters the aneurysm. The experimental results coincided almost perfectly with the simulation results. One small vortex was found at the late systole (Fig. 8c), owing to the non-planarity of the aortic arch. During the early diastole (Fig. 8d), the small vortex turned into a large recirculation region in the center of the aneurysm. However, this high velocity stream, present in the inner wall of curvature, disappeared in the aneurysmal sac which can be associated to the Bernoulli principle, whereby for irrotational flow, the velocity magnitude is inversely proportional to the radius of curvature of the streamline (Tan *et al.*, 2009a; Wood, 1999). A

similar flow pattern was present at the mid-systole (Fig. 8b), but with the extension of high velocity streamline, since the stronger accelerating flow enters the aneurysm. The experimental results coincided almost perfectly with the simulation results. One small vortex was found at the late systole (Fig. 8c), owing to the non-planarity of the aortic arch. During the early diastole (Fig. 8d), the small vortex turned into a large recirculation region in the center of the aneurysm.

Fig. 9(a)-(d) presents the comparison between the experimental and simulated velocity distributions along X and Y directions at the cross-sectional plane $Z=0.012$ m for the aneurysm site. The U-, V- and W-velocity components are presented in line plots to accommodate the quantitative comparison of each velocity components along the overlapping part of the demonstrated lines for each section in the panels. The velocity comparisons in the peak systole reveal minor discrepancies between the experimental and computational results. The CFD calculated velocities showed an average deviation of 11%-36% from the experimentally measured velocities; the highest deviation for U-velocity was along the X-direction with 22%, while along the Y direction there was an average deviation of less than 24%. For the early diastole, the average deviation of CFD calculated velocities from the experimentally measured velocities along the X-direction was calculated to range from 20% to 36%, while for the Y-direction it ranged from 19% to 35% with the highest deviation belonging to the V-velocity component along the Y direction.

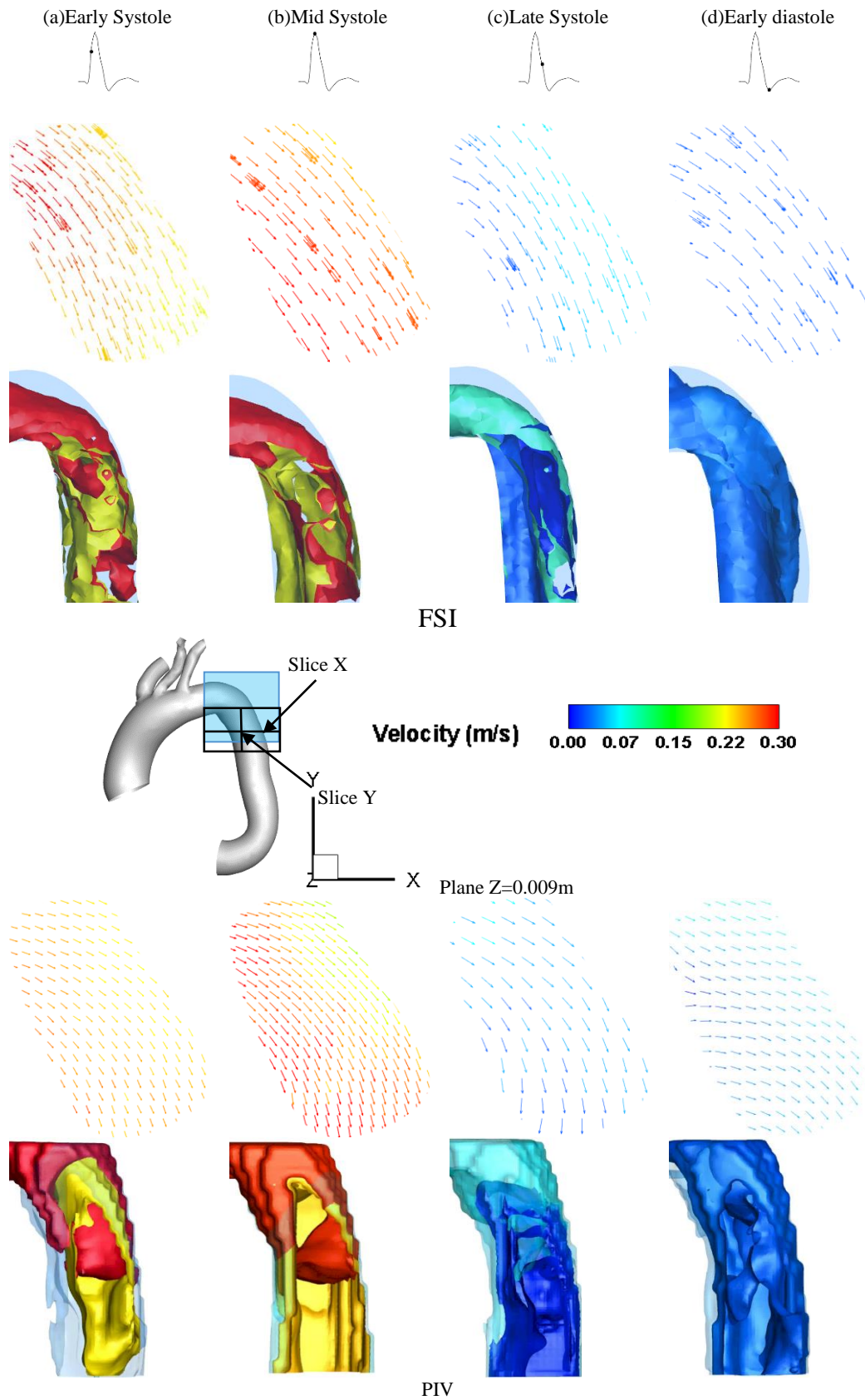


Fig. 6. In-plane velocity pattern and velocity magnitude in isosurface comparisons for the pre-aneurysmal aorta at four different time-points: (a) early systole (b) mid systole (c) late systole (d) early diastole. Upper Panel: numerical results; Lower panel: experimental results.

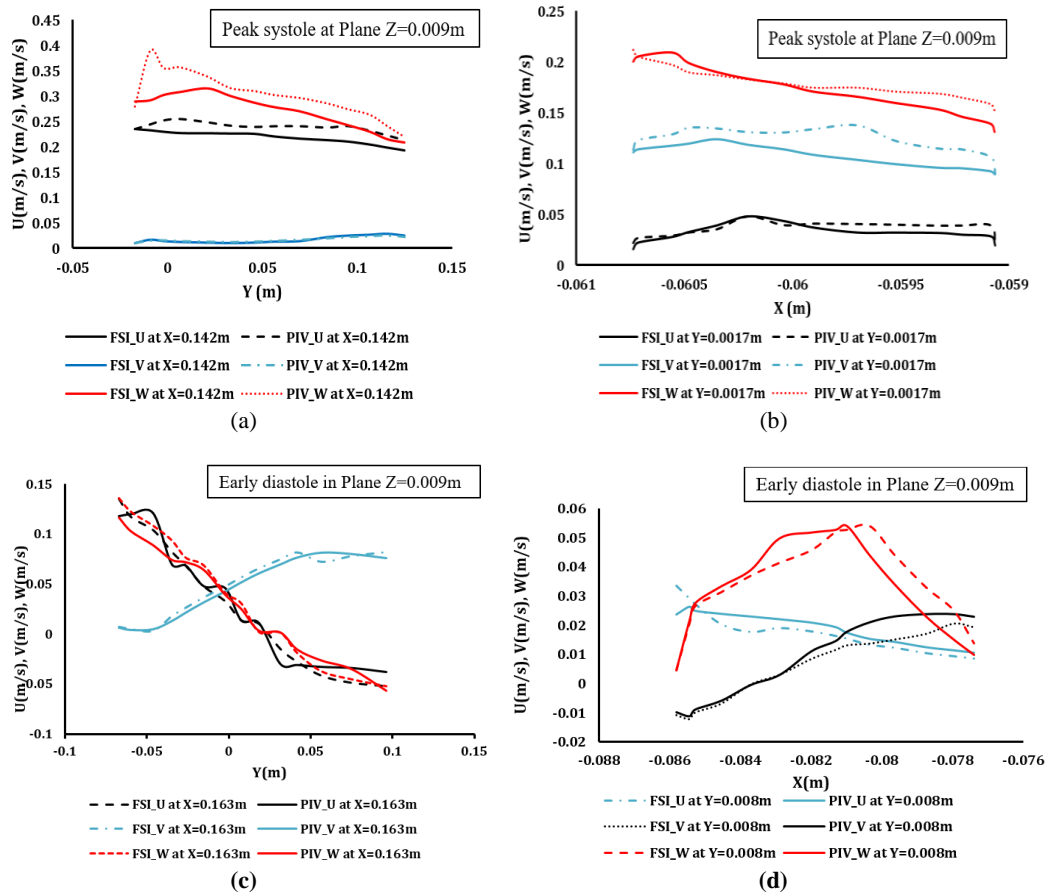


Fig. 7. Comparison of experimental and computational velocity distributions along the planar cross sections across the aortic arch in the pre-aneurysmal model. (a)-(b) peak systole; (c)-(d) early diastole.

Concluding this study, we also present contours of ECAP in Fig. 10 to evaluate the possibility of thrombogenicity. ECAP distribution exhibits a large variation between pre-aneurysmal and post-aneurysmal aorta. Low ECAP (<0.35 Pa) was found on the posterior wall of the pre-aneurysmal aorta, from aortic arch to descending aorta. At the corresponding location in the post-aneurysmal aorta, which turned into the aneurysm, the ECAP value increased from almost zero to 0.35 Pa.

The performance of the solid models was evaluated in stress and strain plot as presented in the Appendix. Large stress and strain were found at the inferior of aortic arch in the post-aneurysmal aorta versus a uniform distribution in the pre-aneurysmal aorta. The location of high stress and strain corresponds well to the location of large recirculation region in the post-aneurysmal aorta.

4. DISCUSSION

This study presents a detailed comparison of flow fields between a 3D fully coupled FSI numerical scheme and PIV experimental measurements with a focus on the hemodynamic changes in the pre-aneurysmal and post-aneurysmal aorta in a thoracic aortic aneurysm model. To the best of our knowledge, very few studies have investigated a 3D

FSI model of aortic aneurysm developed at the descending aorta; and PIV investigation of such model is currently lacking. Most of the prior *in vitro* experiments mainly studied the AAA hemodynamic changes in rigid models (Boutsianis *et al.*, 2009) or with idealized geometry in TAA (Zhang *et al.*, 2014). In the present study, the 3D flow patterns before and after the formation of an aneurysm was characterized in details in compliant wall models with FSI numerical simulations and compared to an *in vitro* PIV experiment.

Numerous *in vivo* and *in-vitro* studies on the hemodynamic change in the healthy aorta are available in the literature. Several computational methods have been able to capture the flow patterns observed in the MRI images. Consistent with the findings of Wen *et al.* (Wen *et al.*, 2010) and Kilner *et al.* (Kilner *et al.*, 1993), in this study we found no flow separation occurring near the inferior aortic arch in the accelerating phase. A small recirculation flow pattern was observed in our FSI investigation in the aortic arch. A similar recirculating vortex was also found in Wen *et al.* (Wen *et al.*, 2010) in a pre-aneurysmal aorta MRI model. However, in our study, this small vortex, skewed toward the descending aortic arch, was detected during the late systole, which can be attributed to the non-planarity of our ascending and descending aorta. The most

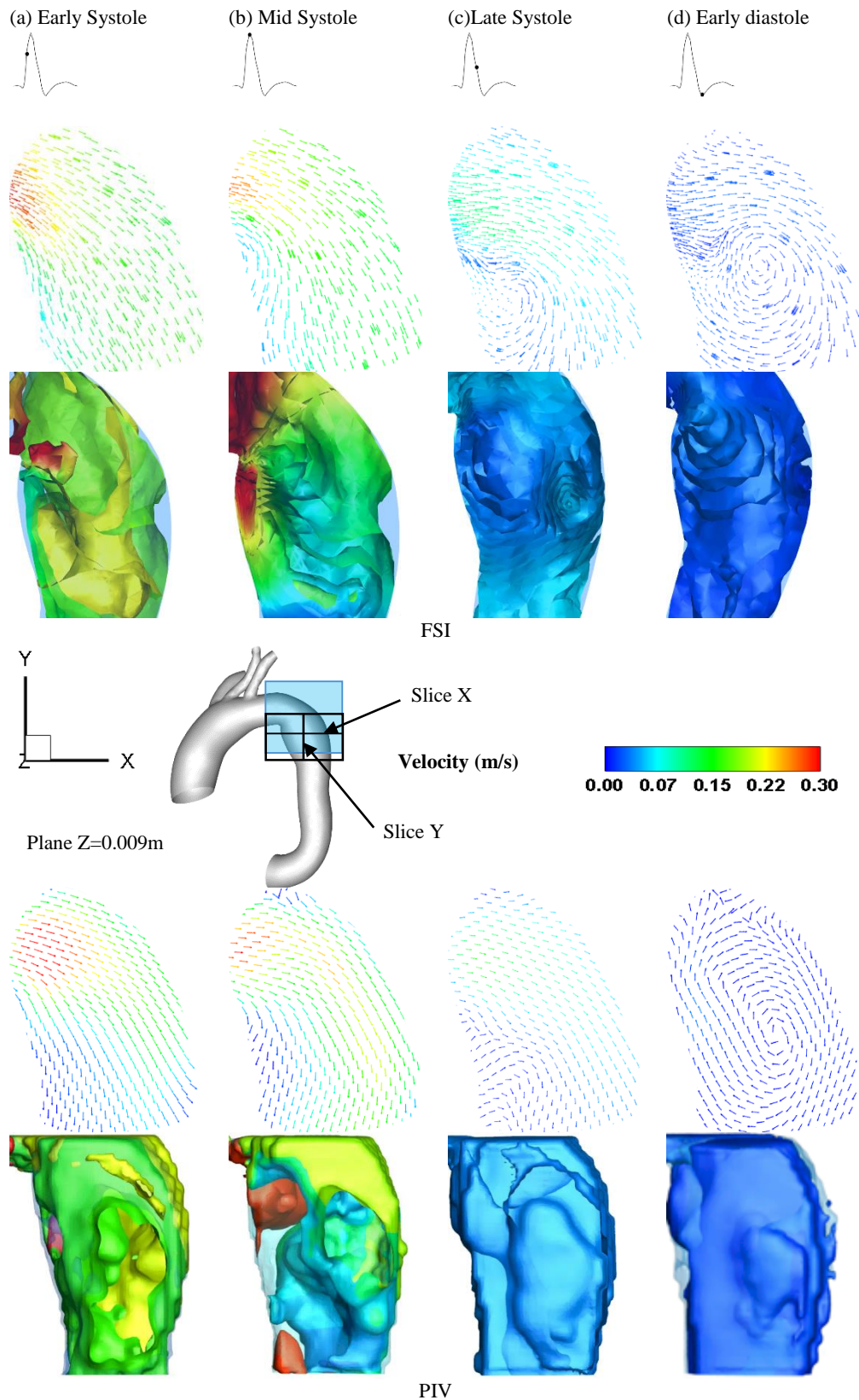


Fig. 8. In-plane velocity pattern and velocity magnitude in isosurface comparisons for the post-aneurysmal aorta at four different time-points: (a) early systole (b) mid systole (c) late systole (d) early diastole. Upper Panel: numerical results; Lower panel: experimental results.

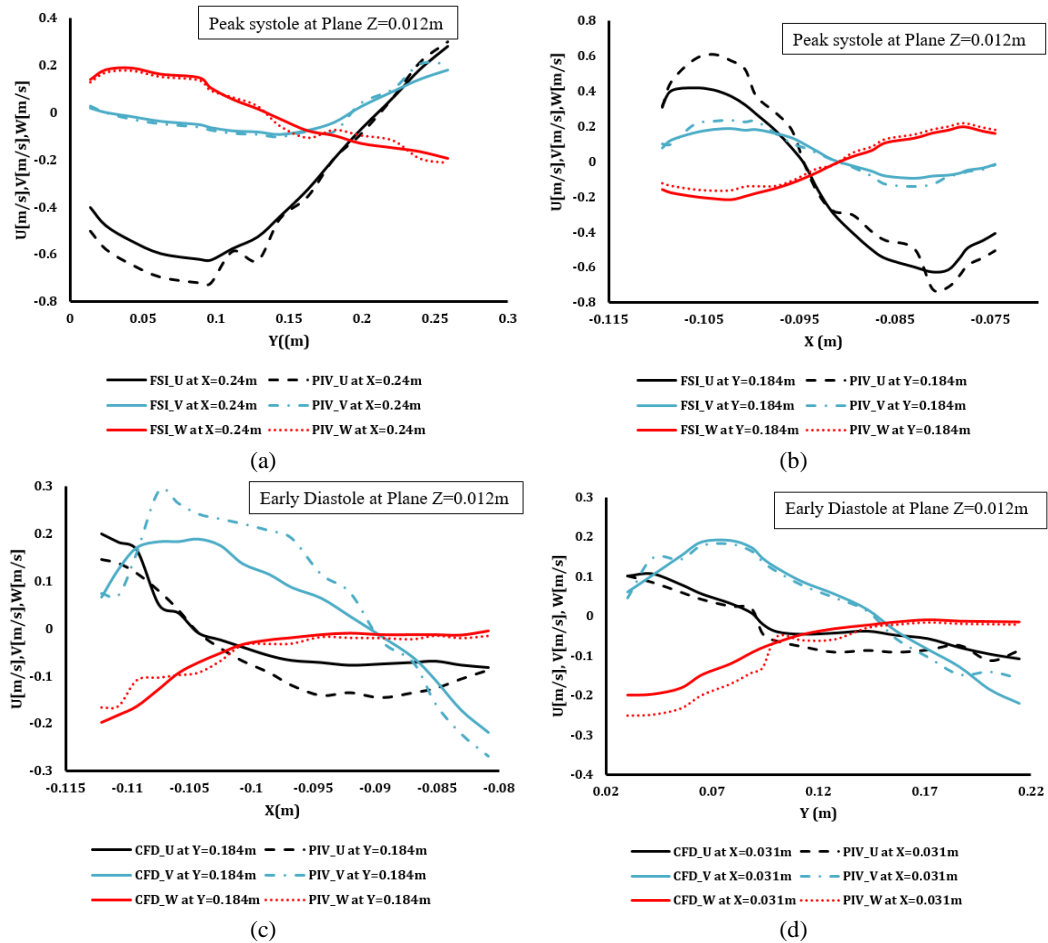


Fig. 9. Comparison of experimental and computational velocity distributions along the planar cross sections across the descending aortic aneurysm. Panels: (a)-(b) peak systole; panels (c)-(d) early diastole.

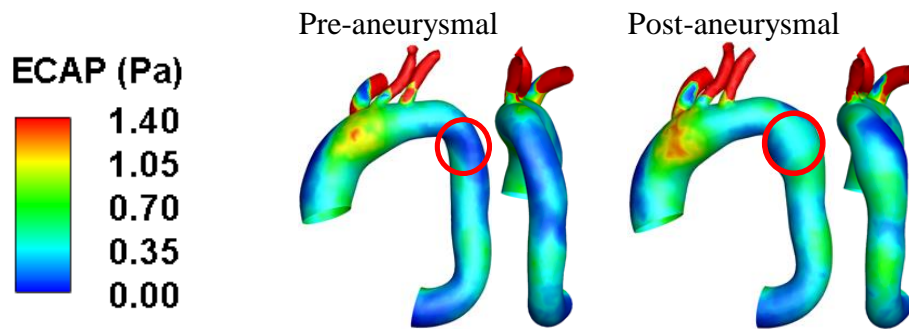


Fig. 10. Endothelial cell activation potential (ECAP) fields shown for both the pre-aneurysmal (left) and post-aneurysmal (right) models.

significant effect of the non-planarity of the pre-aneurysmal aorta is the displacement of the vortices towards the descending aortic arch rather than the upper arch, which is in agreement with observations in healthy subjects (Fujioka and Tanishita, 2000).

From the velocity field results, we observed disturbed flow patterns in the aneurysm sacs, together with a stagnation flow region outside the large recirculation region. The finding of recirculation at the descending aortic aneurysm is in

agreement with MRI findings on similar descending aortic aneurysm (Bogren *et al.*, 1995; Tan *et al.*, 2009b). The presence of large recirculation region that almost filled the whole aneurysmal sac with stagnation flow area may lead to intraluminal thrombus (Arzani *et al.*, 2014). The large recirculation also induced high stress and strain in the inferior region of aortic arch in the post-aneurysmal aorta.

Several studies have reported high ECAP values at

the thrombus site in various geometries (Di Achille *et al.*, 2014; Kandail *et al.*, 2016). ECAP > 1.4 Pa is presumed to have high chance of thrombosis in AAA according to Kelsey *et al.* (Kelsey *et al.*, 2017). In the present study, no extremely high ECAP zone was found in either pre- or post-aneurysmal aorta. It correlates well with the CT images showing no thrombus in original aneurysm. However, the change of ECAP value from 0 Pa to 0.35 Pa, as indicated in Fig. 10, correlated the biomechanical factor to pathophysiology of TAA. Increase of ECAP in the aneurysm can be caused by the repetitive impingement of flow on the aneurysmal wall from the neck of aortic arch. A small vortex constantly exerted shear stress on the wall at the aortic arch in the pre-aneurysmal model, eventually causing a dilation of aneurysm wall, which reduced the overall WSS value, leading to high ECAP value in the post-aneurysmal model. Such change of WSS will enhance the chance of platelet aggregation (Bluestein *et al.*, 1996; Holme *et al.*, 1997) and potentially activates thrombus-causing particles such as platelets and von Willebrand factor (vWF) (Galbusera *et al.*, 1997; Kroll *et al.*, 1996).

The limitation of the current study lies in the uniform thickness of the phantom model. The slight deviation of wall thickness within silicon model at the phantom model can be potentially eliminated with advanced technology for scanning the phantom model such as Magnetic Resonance Imaging (MRI), which will be carried out in the future studies. This methodology was a first and essential step before tapping into clinical applications, such as virtual implantation of medical devices into the aneurysm. This promising research tool can be utilized in developing medical devices for new treatments in patient-specific geometries.

5. CONCLUSION

In the present study, we have investigated hemodynamic changes of the pre-aneurysmal and post-aneurysmal aorta of a patient who endured from a thoracic aortic aneurysm. We have validated the presented FSI model through an equivalent *in vitro* experiment setup. The proposed combined image-based FSI and *in vitro* setup can provide a cost-effective alternative to MRI in assisting medical surgeons in analyzing the flow patterns. This study establishes a cornerstone for further investigation in large cohort medical database that could ultimately transform the use of image-based FSI into clinical medicine.

ACKNOWLEDGEMENT

The authors would like to thank Dr. Munirah from NTU for providing valuable advice for preparation of the manuscript. This project is funded by Singapore Ministry of Education Tier 1 Grant (R-397-000-266-114) and Singapore-China Joint Research Programme (Project No. 1610500025). The authors also would like to thank AUN/SEED-Net JICA for providing scholarship to the student.

REFERENCES

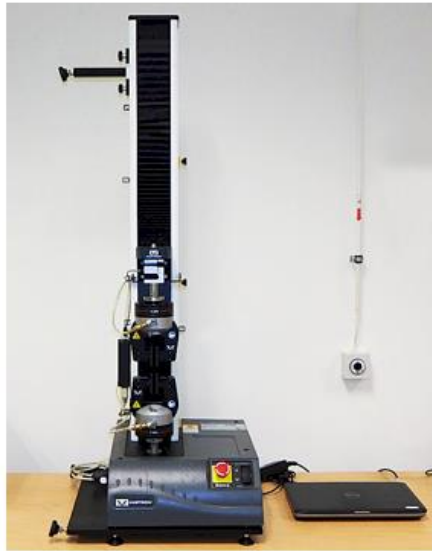
- Arzani, A., G. Y. Suh, R. L. Dalman and S. C. Shadden (2014). A longitudinal comparison of hemodynamics and intraluminal thrombus deposition in abdominal aortic aneurysms. *American Journal of Physiology - Heart and Circulatory Physiology* 307(12): H1786–H1795.
- Biasetti, J., F. Hussain and T. C. Gasser (2011). Blood flow and coherent vortices in the normal and aneurysmatic aortas: a fluid dynamical approach to intra-luminal thrombus formation. *Journal of The Royal Society Interface* 8, 1449-1461.
- Bluestein, D., L. Niu, R. Schoepfoerster and M. Dewanjee (1996). Steady flow in an aneurysm model: correlation between fluid dynamics and blood platelet deposition. *Journal of biomechanical engineering* 118, 280-286.
- Bogren, H. G., R. H. Mohiaddin, G. Z. Yang, P. J. Kilner and D.N. Firmin (1995). Magnetic resonance velocity vector mapping of blood flow in thoracic aortic aneurysms and grafts. *The Journal of thoracic and cardiovascular surgery* 110, 704-714.
- Borghi, A., N. B. Wood, R. H. Mohiaddin and X. Y. Xu (2008). Fluid–solid interaction simulation of flow and stress pattern in thoracoabdominal aneurysms: A patient-specific study. *Journal of Fluids and Structures* 24, 270-280.
- Boutsianis, E., M. Guala, U. Olgac, S. Wildermuth, K. Hoyer, Y. Ventikos and D. Poulikakos (2009). CFD and PTV steady flow investigation in an anatomically accurate abdominal aortic aneurysm. *Journal of Biomechanical Engineering* 131, 011008.
- Chandra, S., S. S. Raut, A. Jana, R. W. Biederman, M. Doyle, S. C. Muluk and E. A. Finol (2013). Fluid-structure interaction modeling of abdominal aortic aneurysms: the impact of patient-specific inflow conditions and fluid/solid coupling. *Journal of Biomechanical Engineering* 135, 0810011-08100114.
- Corbett, T., B. Doyle, A. Callanan, M. Walsh and T. McGloughlin (2010). Engineering silicone rubbers for *in vitro* studies: creating AAA models and ILT analogues with physiological properties. *Journal of biomechanical engineering* 132, 011008.
- Di Achille, P., G. Tellides, C. A. Figueroa, J. D. Humphrey (2014). A haemodynamic predictor of intraluminal thrombus formation in abdominal aortic aneurysms. *Proceedings of the Royal Society A: Mathematical, Physical and Engineering Science* 470.
- Doyle, B. J., T. M. McGloughlin, E. G. Kavanagh, P. R. Hoskins (2014). From detection to rupture: a serial computational fluid dynamics case study of a rapidly expanding, patient-specific, ruptured abdominal aortic aneurysm. *In Computational Biomechanics for Medicine*. New York, NY.

- Drewe, C. J., L. P. Parker, L. J. Kelsey, P. E. Norman, J. T. Powell and B. J. Doyle (2017). Haemodynamics and stresses in abdominal aortic aneurysms: A fluid-structure interaction study into the effect of proximal neck and iliac bifurcation angle. *Journal of Biomechanics* 60, 150-156.
- Elefteriades, J. A. and E. A. Farkas (2010). Thoracic aortic aneurysm clinically pertinent controversies and uncertainties. *Journal of the American College of Cardiology* 55, 841-857.
- Finol, E. A. and C. H. Amon (2001). Blood Flow in Abdominal Aortic Aneurysms: Pulsatile Flow Hemodynamics. *Journal of Biomechanical Engineering* 123, 474-484.
- Fujioka, H. and K. Tanishita (2000). Computational fluid mechanics of the blood flow in an aortic vessel with realistic geometry, in: Yamaguchi, T. (Ed.), *Clinical Application of Computational Mechanics to the Cardiovascular System*. Springer Japan, Tokyo, 99-117.
- Fung, Y. C. (2013). *Biomechanics: Circulation*. Springer New York.
- Galbusera, M., C. Zoja, R. Donadelli, S. Paris, M. Morigi, A. Benigni, M. Figliuzzi, G. Remuzzi and A. Remuzzi (1997). Fluid shear stress modulates von Willebrand factor release from human vascular endothelium. *Blood* 90, 1558-1564.
- Gao, F., Z. Guo, M. Sakamoto and T. Matsuzawa (2006). Fluid-structure interaction within a layered aortic arch model. *Journal of biological physics* 32, 435-454.
- Holme, P. A., U. Orvim, M. J. Hamers, N. O. Solum, F. R. Brosstad, R. M. Barstad and K. S. Sakariassen (1997). Shear-induced platelet activation and platelet microparticle formation at blood flow conditions as in arteries with a severe stenosis. *Arteriosclerosis, thrombosis, and vascular biology* 17, 646-653.
- Kabinejadian, F., F. Cui, B. Su, A. Danpinid, P. Ho, H. L. Leo (2015). Effects of a carotid covered stent with a novel membrane design on the blood flow regime and hemodynamic parameters distribution at the carotid artery bifurcation. *Medical & biological engineering & computing* 53, 165-177.
- Kabinejadian, F., M. Kaabi Nezhadian, F. Cui, P. Ho and H.L. Leo (2016). Covered stent membrane design for treatment of atheroembolic disease at carotid artery bifurcation and prevention of thromboembolic stroke: an in vitro experimental study. *Artificial organs* 40, 159-168.
- Kandail, H., M. Hamady and X. Y. Xu (2016). Effect of a Flared Renal Stent on the Performance of Fenestrated Stent-Grafts at Rest and Exercise Conditions. *Journal of Endovascular Therapy* 23, 809-820.
- Kelsey, L. J., J. T. Powell, P. E. Norman, K. Miller and B. J. Doyle (2017). A comparison of hemodynamic metrics and intraluminal thrombus burden in a common iliac artery aneurysm. *International journal for numerical methods in biomedical engineering* 33, e2821.
- Kilner, P. J., G. Z. Yang, R. H. Mohiaddin, D. N. Firmin and D. B. Longmore (1993). Helical and retrograde secondary flow patterns in the aortic arch studied by three-directional magnetic resonance velocity mapping. *Circulation* 88, 2235-2247.
- Kroll, M. H., J. D. Hellums, L. McIntire, A. Schafer and J. Moake (1996). Platelets and shear stress. *Blood* 88, 1525-1541.
- Lantz, J., J. Renner and M. Karlsson (2011). Wall shear stress in a subject specific human aorta— influence of fluid-structure interaction. *International Journal of Applied Mechanics* 3, 759-778.
- Li, Z. and C. Kleinstreuer (2006). Computational analysis of type II endoleaks in a stented abdominal aortic aneurysm model. *Journal of Biomechanics* 39, 2573-2582.
- Li, Z. and C. Kleinstreuer (2007). A comparison between different asymmetric abdominal aortic aneurysm morphologies employing computational fluid-structure interaction analysis. *European Journal of Mechanics-B/Fluids* 26, 615-631.
- Menichini, C., Z. Cheng, R. G. Gibbs and X. Y. Xu (2018). A computational model for false lumen thrombosis in type B aortic dissection following thoracic endovascular repair. *Journal of biomechanics* 66, 36-43.
- Mesri, Y., H. Niazmand and A. Deyranlou (2017). Numerical Study on Fluid-Structure Interaction in a Patient-Specific Abdominal Aortic Aneurysm for Evaluating Wall Heterogeneity and Material Model Effects on its Rupture. *Journal of Applied Fluid Mechanics*.
- Morris, L., P. Delassus, A. Callanan, M. Walsh, F. Wallis, P. Grace and T. McGloughlin (2005). 3-D numerical simulation of blood flow through models of the human aorta. *Journal of biomechanical engineering* 127, 767-775.
- Olufsen, M. S., C. S. Peskin, W. Y. Kim, E. M. Pedersen, A. Nadim and J. Larsen (2000). Numerical simulation and experimental validation of blood flow in arteries with structured-tree outflow conditions. *Annals of biomedical engineering* 28, 1281-1299.
- Pedley, T. J. (2003). Mathematical modelling of arterial fluid dynamics. *Journal of engineering mathematics* 47, 419-444.
- Rissland, P., Y. Alemu, S. Einav, J. Ricotta and D. Bluestein (2008). Abdominal Aortic Aneurysm Risk of Rupture: Patient-Specific FSI Simulations Using Anisotropic Model. *Journal of Biomechanical Engineering* 131, 031001-031001-031010.

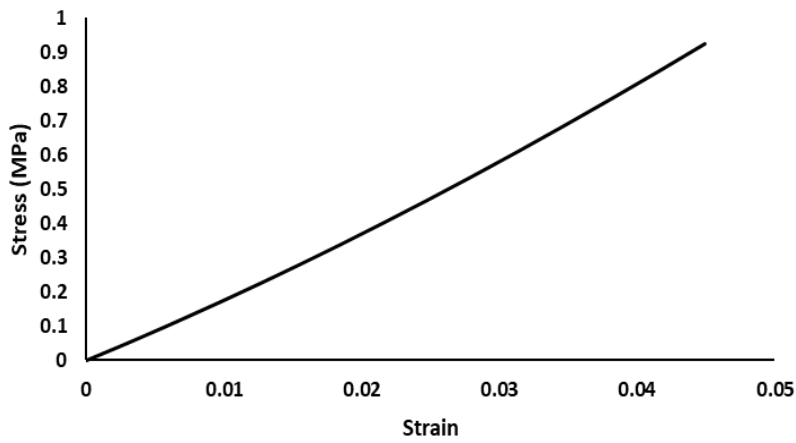
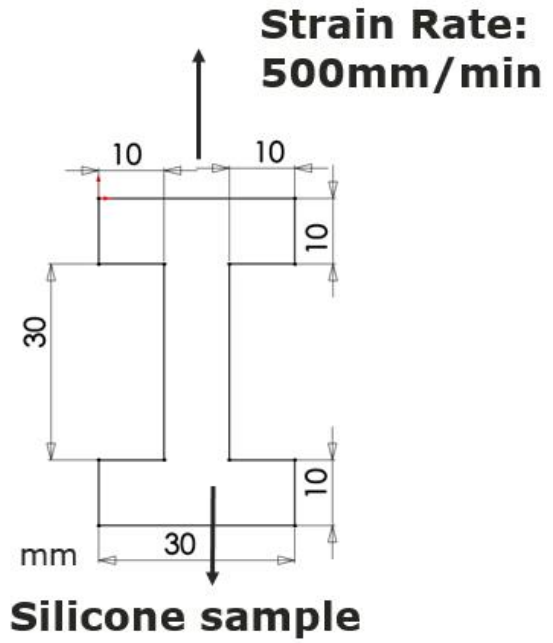
- Scotti, C. M., J. Jimenez, S. C. Muluk and E. A. Finol (2008). Wall stress and flow dynamics in abdominal aortic aneurysms: finite element analysis vs. fluid–structure interaction. *Computer Methods in Biomechanics and Biomedical Engineering* 11, 301-322.
- Sekhar, L. N. and R. C. Heros (1981). Origin, growth, and rupture of saccular aneurysms: a review. *Neurosurgery* 8, 248-260.
- Shahcheraghi, N., H. A. Dwyer, A. Y. Cheer, A. I. Barakat and T. Rutaganira (2002). Unsteady and Three-Dimensional Simulation of Blood Flow in the Human Aortic Arch. *Journal of Biomechanical Engineering* 124, 378-387.
- Soudah, E., G. Vilalta, J. Vilalta, M. Bordone, F. Nieto, M. Pérez, C. Vaquero Puerta (2012). Idealized Abdominal Aortic Aneurysm (AAA) Geometry as Predictor of Hemodynamics Stresses, European Congress on Computational Methods in Applied Sciences and Engineering (ECCOMAS 2012) Vienna, Austria.
- Steinman, D. A. (2002). Image-Based Computational Fluid Dynamics Modeling in Realistic Arterial Geometries. *Annals of Biomedical Engineering* 30, 483-497.
- Tan, F., A. Borghi, R. Mohiaddin, N. Wood, S. Thom and X. Xu (2009a). Analysis of flow patterns in a patient-specific thoracic aortic aneurysm model. *Computers & Structures* 87, 680-690.
- Tan, F. P. P., R. Torii, A. Borghi, R. H. Mohiaddin, N. B. Wood and X. Y. Xu (2009b). Fluid structure interaction analysis of wall stress and flow patterns in a thoracic aortic aneurysm. *International Journal of Applied Mechanics* 01, 179-199.
- Tse, K. M., P. Chiu, H. P. Lee and P. Ho (2011). Investigation of hemodynamics in the development of dissecting aneurysm within patient-specific dissecting aneurysmal aortas using computational fluid dynamics (CFD) simulations. *Journal of biomechanics* 44, 827-836.
- Wang, X. and X. Li (2011). Computational simulation of aortic aneurysm using FSI method: Influence of blood viscosity on aneurysmal dynamic behaviors. *Computers in biology and medicine* 41, 812-821.
- Wen, C. Y., A. S. Yang, L. Y. Tseng and J. W. Chai (2010). Investigation of Pulsatile Flowfield in Healthy Thoracic Aorta Models. *Annals of Biomedical Engineering* 38, 391-402.
- Wolters, B., M. Rutten, G. Schurink and F. van de Vosse (2010). Computational modelling of endoleak after endovascular repair of abdominal aortic aneurysms. *International Journal for Numerical Methods in Biomedical Engineering* 26, 322-335.
- Wolters, B. J. B. M., M. C. M. Rutten, G. W. H. Schurink, U. Kose, J. de Hart and F. N. van de Vosse (2005). A patient-specific computational model of fluid–structure interaction in abdominal aortic aneurysms. *Medical Engineering & Physics* 27, 871-883.
- Wood, N. (1999). Aspects of fluid dynamics applied to the larger arteries. *Journal of theoretical biology* 199, 137-161.
- Xenos, M., N. Labropoulos, S. Rambhia, Y. Alemu, S. Einav, A. Tassiopoulos, N. Sakalihan and D. Bluestein (2015). Progression of abdominal aortic aneurysm towards rupture - refining clinical risk assessment using a fully coupled fluid-structure interaction method. *Annals of biomedical engineering* 43, 139-153.
- Zambrano, B. A., H. Gharahi, C. Lim, F. A. Jaber, J. Choi, W. Lee and S. Baek (2016). Association of intraluminal thrombus, hemodynamic forces, and abdominal aortic aneurysm expansion using longitudinal CT images. *Annals of biomedical engineering* 44, 1502-1514.
- Zhang, P., X. Liu, A. Sun, Y. Fan and X. Deng (2015). Hemodynamic insight into overlapping bare-metal stents strategy in the treatment of aortic aneurysm. *Journal of biomechanics* 48, 2041-2046.
- Zhang, P., A. Sun, F. Zhan, J. Luan and X. Deng (2014). Hemodynamic study of overlapping bare-metal stents intervention to aortic aneurysm. *Journal of Biomechanics* 47, 3524-3530.

Appendix – Stress and Strain for the Solid Model

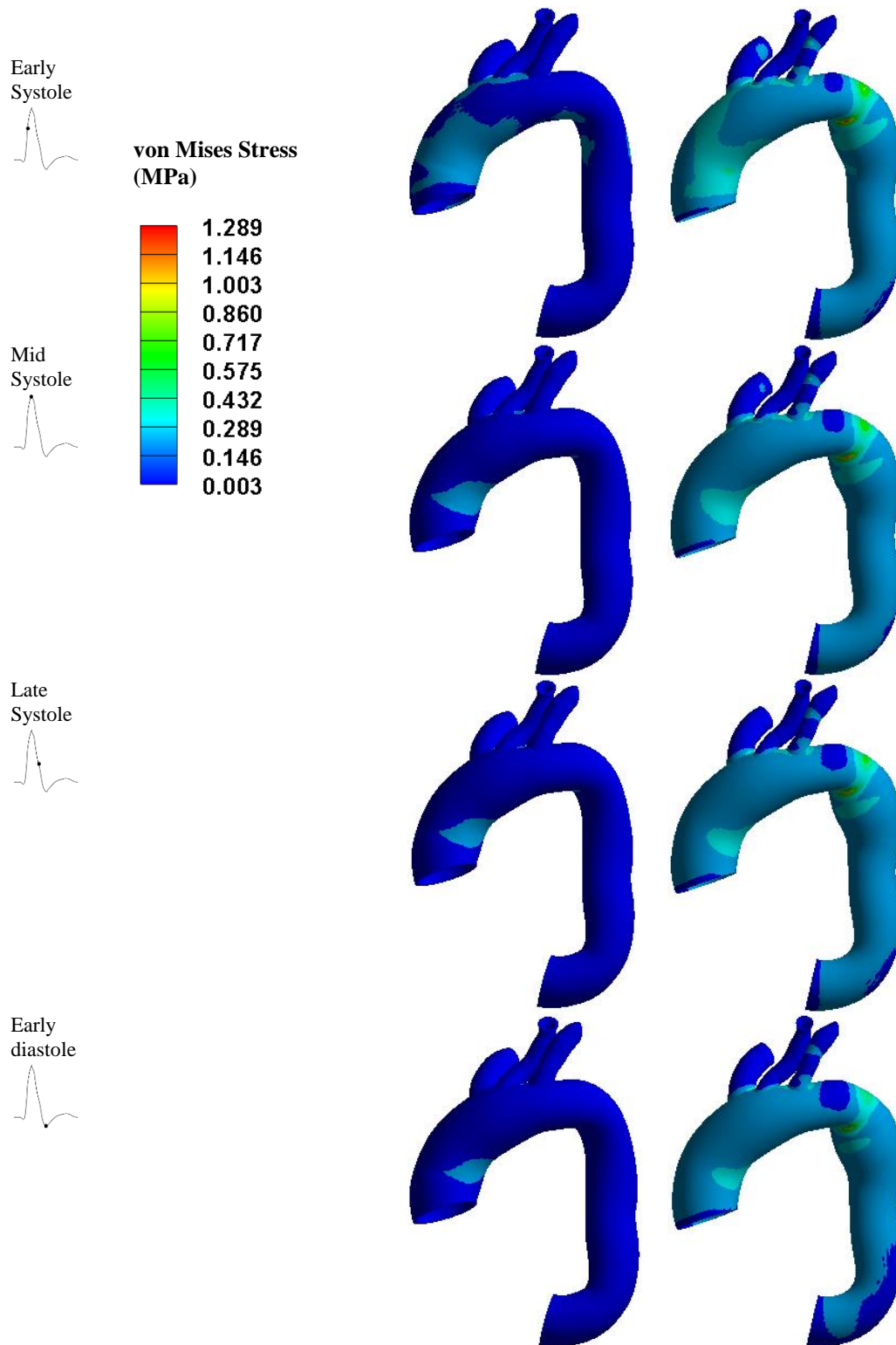
Young modulus 2MPa was calculated from the uniaxial tensional stress and strain plot as shown in the following figure



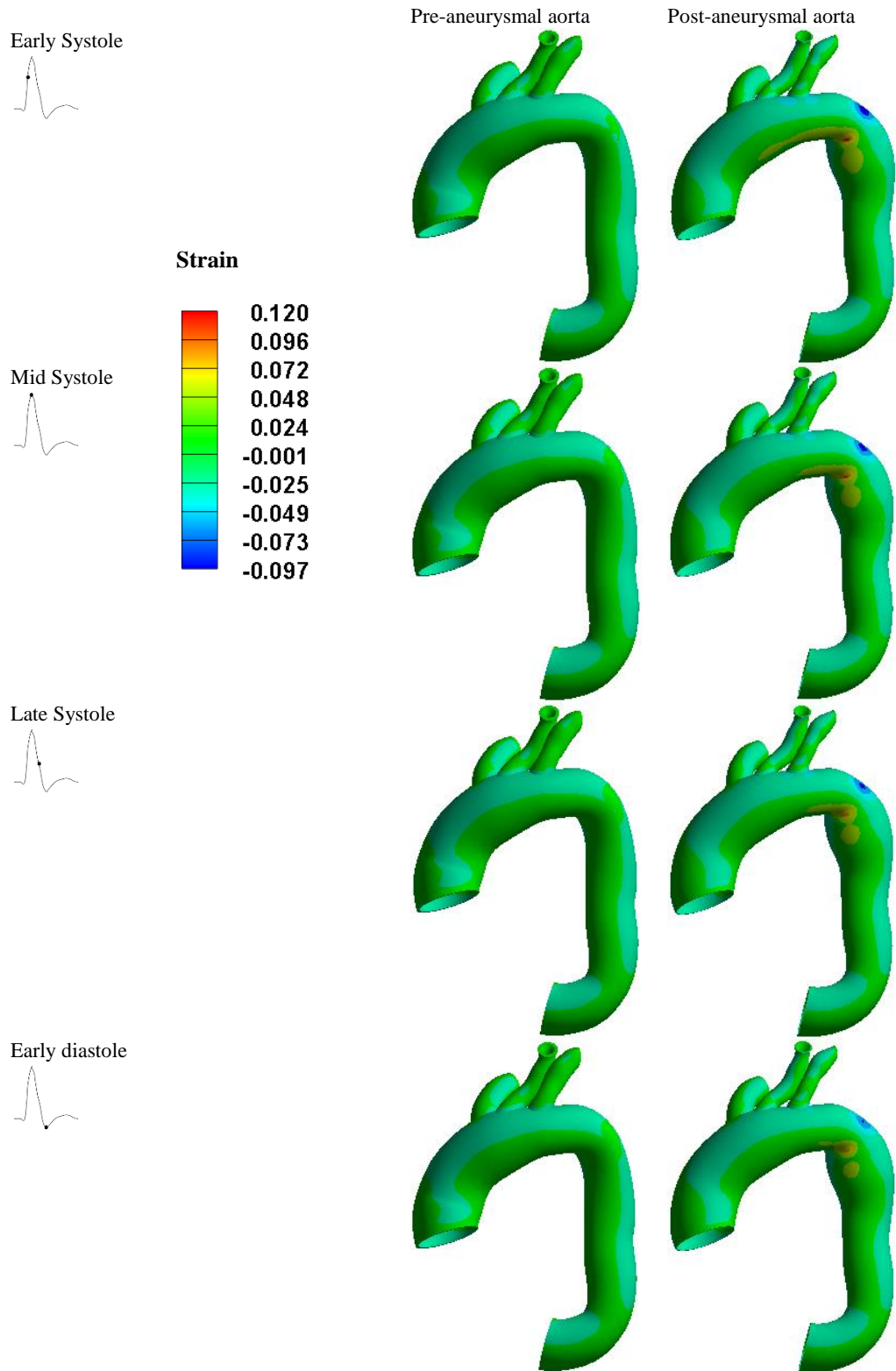
Instron 3343



von Mises stress plot



Shear strain plot



Deformation plot

